

Gap and magnetic engineering via doping and pressure in tuning the colossal magnetoresistance in $(\text{Mn}_{1-x}\text{Mg}_x)_3\text{Si}_2\text{Te}_6$

Chaoxin Huang,¹ Mengwu Huo,¹ Xing Huang,¹ Hui Liu,¹ Lisi Li,¹ Ziyu Zhang,² Zhiqiang Chen,² Yifeng Han,³ Lan Chen,¹ Feixiang Liang,¹ Hongliang Dong,² Bing Shen,¹ Hualei Sun,^{4,*} and Meng Wang^{1,†}

¹*Center for Neutron Science and Technology, Guangdong Provincial Key Laboratory of Magnetoelectric Physics and Devices, School of Physics, Sun Yat-Sen University, Guangzhou 510275, China*

²*Center for High Pressure Science and Technology Advanced Research, Shanghai 201203, China*

³*Center for Materials of the University, School of Molecular Sciences, Arizona State University, Tempe, Arizona 85287, USA*

⁴*School of Science, Sun Yat-Sen University, Shenzhen 518107, China*

Ferrimagnetic nodal-line semiconductor $\text{Mn}_3\text{Si}_2\text{Te}_6$ keeps the records of colossal magnetoresistance (CMR) and angular magnetoresistance (AMR). Here we report tuning the electronic transport properties via doping and pressure in $(\text{Mn}_{1-x}\text{Mg}_x)_3\text{Si}_2\text{Te}_6$. As the substitution of nonmagnetic Mg^{2+} for magnetic Mn^{2+} , ferrimagnetic transition temperature T_C gradually decreases, while the resistivity increases significantly. At the same time, the CMR and AMR are both enhanced for the low-doping compositions (e.g., $x = 0.1$ and 0.2), which can be attributed to doping-induced broadening of the band gap and a larger variation range of the resistivity when undergoing a metal-insulator transition by applying a magnetic field along the c axis. On the contrary, T_C rises with increasing pressure due to the enhancement of the magnetic exchange interactions until a structural transition occurs at ~ 13 GPa. Meanwhile, the activation gap is lowered under pressure and the magnetoresistance is decreased dramatically above 6 GPa where the gap is closed. At 20 and 26 GPa, evidences for a superconducting transition at ~ 5 K are observed. The results reveal that doping and pressure are effective methods to tune the activation gap, and correspondingly, the CMR and AMR in nodal-line semiconductors, providing an approach to investigate the magnetoresistance materials for novel spintronic devices.

PACS numbers:

I. INTRODUCTION

Since giant magnetoresistance was discovered in magnetic multilayers, the spin-charge coupling has been widely investigated for decades in a number of fields, including magnetic storage, magnetic sensor, magnetometer and so on¹⁻⁶. CMR is more sensitive to a magnetic field than giant magnetoresistance, whose variation in resistance can be close to 100%. CMR was first reported in doped manganese perovskite, where the double exchange mechanism and dynamic Jahn-Teller effect were demonstrated to play a key role⁷⁻⁹. Other mechanisms were suggested for the later discovered CMR materials, such as strong magnetic fluctuations in EuCd_2P_2 ¹⁰, magnetic polarons in $\text{Ti}_2\text{Mn}_2\text{O}_7$ ^{11,12} and $\text{Eu}_5\text{In}_2\text{Sb}_6$ ¹³, and spin-orbit coupling/spin-texture driven CMR in EuTe_2 and EuMnSb_2 ¹⁴⁻¹⁶. Two-dimensional (2D) layered materials have higher spatial anisotropy, which is a fertile ground to explore new material systems with CMR and AMR^{16,17}.

Indeed, the quasi-2D ferrimagnetic (FIM) semiconductor $\text{Mn}_3\text{Si}_2\text{Te}_6$ was found to exhibit the largest CMR and AMR, where the resistivity decreases by 10^7 as defined by $(\rho_H - \rho_0)/\rho_H$ for $H \parallel c$ axis, but changes slightly in resistivity when H is along the ab plane¹⁸⁻²⁴. It was suggested that the nodal-line degeneracy of $\text{Mn}_3\text{Si}_2\text{Te}_6$ can be controlled by spin orientation. When the applied field is along the c axis, spin-orbit coupling (SOC) between Mn and Te will result in band splitting and one of the bands will shift toward the Fermi level, leading to the

closing of the electric gap and metal-insulator transition (MIT)²⁰. Later, chiral orbital currents (COC) were suggested to circulate along the edges of MnTe_6 octahedra. In this scenario, the coupling between the spin of Mn^{2+} and the effective moments of the COC could reduce the electron scattering when a magnetic field is applied along the c axis²⁵. However, single-crystal neutron diffraction and magnetization measurements reveal that the applied field along the c axis smoothly tilts the magnetic moment during the CMR occurs^{19,20,26}. The activation gap may be a key gradient in the mechanism. Thus, further research to improve the magnitudes of the CMR and AMR and elucidate the mechanism is crucial to promote potential applications in the future.

Doping and pressure are considered as effective methods to tune quantum transport properties in electronic correlated materials²⁷⁻³². In this work, we report the successful synthesis of a series of $(\text{Mn}_{1-x}\text{Mg}_x)_3\text{Si}_2\text{Te}_6$ single crystals from $x = 0$ to 1.0 at 0.1 intervals and investigations of the evolutions of structure, magnetism, and electric transport properties with doping and pressure. We find the Mg-doping can suppress the FIM, increase the resistivity by enlarging the activation gap, and enhance the CMR and AMR by about two orders of magnitude compared to the undoped compound. On the other hand, pressure induces the closure of the thermal activation gap at ~ 7.0 GPa accompanied by the disappearance of the CMR, a structural transition at 14.6 GPa, and a superconducting transition at 5 K and 20 GPa. Our re-

sults reveal that the nodal-line topological band gap can be widened or narrowed by doping or applying pressure, thus tuning the CMR and AMR to a required magnitude.

II. EXPERIMENTAL DETAILS

Single crystals of $(\text{Mn}_{1-x}\text{Mg}_x)_3\text{Si}_2\text{Te}_6$ ($0 \leq x \leq 1$) were grown by the self-flux method and characterized by x-ray diffraction (XRD, Empyrean), energy dispersive x-ray spectroscopy (EDS, EVO Zeiss), Laue diffractometer (Photonic Science), and physical property measurement system (PPMS, Quantum Design). For partial samples with resistance exceeding the measuring range (e.g., data for $x = 0.1$ at low temperature and low field), an external voltmeter (Keithley) was employed while necessary.

High-pressure electrical transport measurements of $\text{Mn}_3\text{Si}_2\text{Te}_6$ single crystals were carried out using a miniature diamond anvil cell (DAC) made from a Be-Cu alloy on the PPMS. Diamond anvils with a $300 \mu\text{m}$ culet were used. The corresponding sample chamber with a $110 \mu\text{m}$ diameter was made in an insulating gasket achieved by cubic boron nitride and epoxy mixture. KBr powders were employed as the pressure-transmitting medium, providing a quasi-hydrostatic environment. The pressure was calibrated by measuring the shift of the fluorescence wavelength of the ruby sphere, which was loaded in the sample chamber. The standard four-probe technique was adopted for these measurements.

The in situ high-pressure synchrotron powder XRD patterns were collected at 300 K with an x-ray wavelength of 0.6199 \AA on the Shanghai Synchrotron Radiation Facility. A symmetric DAC with a pair of $300 \mu\text{m}$ diameter culet was used. The sample chamber was drilled by laser with a diameter of $120 \mu\text{m}$. Daphne oil was used as the pressure-transmitting medium, and the pressure in the DAC was also calibrated by the shift of the fluorescence of the ruby sphere. The high-pressure XRD data were initially integrated using Dioptas³³ (with a CeO₂ calibration) and fitted using the Pawley method in Topas-Academic V6 software³⁴.

III. RESULTS AND DISCUSSION

XRD measurements reveal that the crystal structure of $(\text{Mn}_{1-x}\text{Mg}_x)_3\text{Si}_2\text{Te}_6$ ($0 \leq x \leq 1$) preserves the trigonal space group $P\bar{3}1c$. A small number of impurities of MnTe_2 can be identified in the XRD patterns of $x = 0$ and 0.4 compounds³⁵. The lattice parameters are smoothly enlarged as the Mg doping. The nominal compositions are close to the EDS-determined compounds [Supplementary Fig. S1]. We use the nominal x to indicate the composition of $(\text{Mn}_{1-x}\text{Mg}_x)_3\text{Si}_2\text{Te}_6$ through out this paper.

Figure 1 shows the doping effects on magnetization and resistivity of $(\text{Mn}_{1-x}\text{Mg}_x)_3\text{Si}_2\text{Te}_6$. The temperature

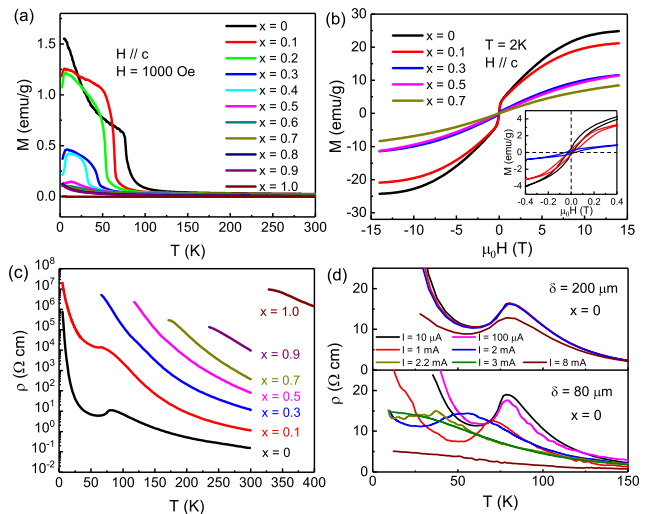


FIG. 1: (a) Temperature dependence of magnetization of $(\text{Mn}_{1-x}\text{Mg}_x)_3\text{Si}_2\text{Te}_6$ with the magnetic field parallel to the c axis and $H = 1000 \text{ Oe}$. (b) Temperature dependence of magnetization of $(\text{Mn}_{1-x}\text{Mg}_x)_3\text{Si}_2\text{Te}_6$ at 2 K with an applied field parallel to the c axis from -14 to 14 T . The inset shows the hysteresis loops of the $x = 0, 0.1,$ and 0.3 samples at low fields. (c) Temperature dependence of resistivity of $(\text{Mn}_{1-x}\text{Mg}_x)_3\text{Si}_2\text{Te}_6$. The resistivity of the $x = 1.0$ sample was measured from 328 to 400 K due to the large magnitude which exceeded the measurement range at lower temperatures. (d) Temperature dependence of resistivity of $\text{Mn}_3\text{Si}_2\text{Te}_6$ with thicknesses of 200 and $80 \mu\text{m}$ measured with various currents.

dependence of magnetization in Fig. 1(a) reveals a transition at $\sim 78 \text{ K}$ for $\text{Mn}_3\text{Si}_2\text{Te}_6$ that is consistent with the reported FIM order^{36–39}. The FIM order is progressively suppressed with increasing doping until the disappearance for $x > 0.5$. In addition to the FIM transition, an abnormal decline on the magnetization curve can be observed at low temperatures for $0.1 \leq x \leq 0.5$, which could be ascribed to a spin reorientation transition due to a doping-induced magnetic dilution (Supplementary Fig. S2)⁴⁰. The saturation magnetization decreases with increasing x [Fig. 1(b)]. The hysteresis loops resulting from the FIM can be observed in the low field range in both the undoped and doped samples [see inset in Fig. 1(b)].

Temperature dependence of the resistivity for different compositions is displayed in Fig. 1(c). Anomalies on the resistivity of $x = 0$ and 0.1 samples correspond to the T_C s. When the x exceeds 0.1 , the anomaly associated with T_C cannot be observed due to the limit of the measured resistance range. The values of the resistivity increase from 10^{-1} to $10^7 \Omega \text{ cm}$ at $\sim 300 \text{ K}$ in the doping range of $0 \leq x \leq 1$. The resistivity for $\text{Mg}_3\text{Si}_2\text{Te}_6$ is too large to be measured below 328 K in our experimental setup⁴¹. We fit the resistivity above T_C using the polaron hopping model³⁹ $\rho(T) = AT \exp(E_a/k_B T)$, where E_a is the activation energy and k_B is the Boltzmann constant. The results reveal linearly increased E_a from 83.5

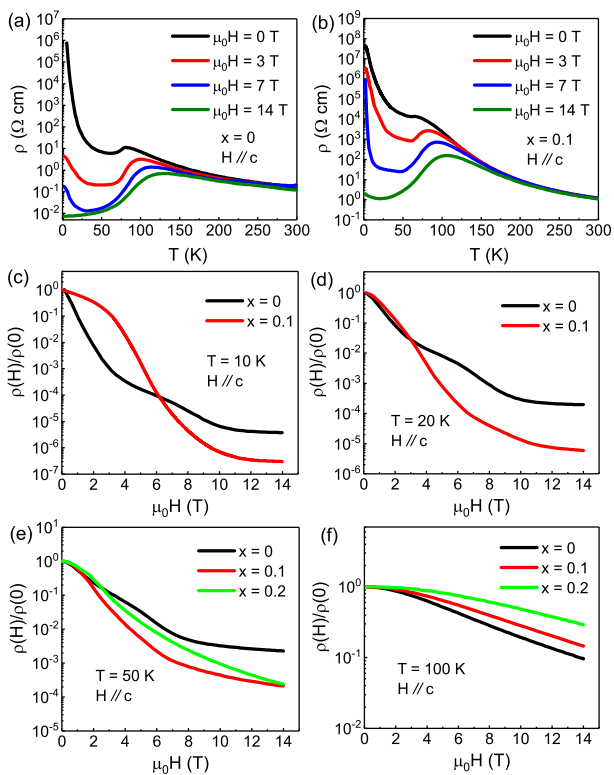


FIG. 2: (a) Resistivity as a function of temperature in different magnetic fields parallel to the c axis for the undoped sample and (b) for the $x = 0.1$ sample. (c) Field dependence of ρ_H/ρ_0 for the samples of $x = 0$ and 0.1 at 10 K, (d) 20 K, and for the samples of $x = 0, 0.1,$ and 0.2 at (e) 50 K and (f) 100 K.

to 408.6 meV with the Mg^{2+} doping [Fig. 5], revealing that the gap changes uniformly as doping, which may facilitate the electronic structure tuning in real applications. Figure 1(d) shows the resistivity measurements on $\text{Mn}_3\text{Si}_2\text{Te}_6$ single crystals with different currents and thicknesses. The T_C can be tuned by the magnitude of current for the single crystal with a thickness of $\sigma = 80$ μm , consistent with the previously proposed COC state²⁵. However, the anomalies in resistivity for the $\sigma = 200$ μm sample are hardly changed until the current I is up to 8 mA. According to the discrepancy of the T_C s for different currents and samples, the COC state does not depend on the current magnitude but the current density. The critical current density for the FIM state at 0 K is estimated to be 95 mA/mm² [Supplementary Fig. S1(d)].

To reveal the doping effect on the CMR, we show the temperature dependence of resistivity with magnetic fields parallel to the c axis for the undoped $x = 0$ and doped $x = 0.1$ compounds in Figs. 2(a) and 2(b). They all exhibit large CMR below the T_C . Similar measurements on the $x = 0.2, 0.3, 0.5,$ and 0.7 compositions are shown in the Supplementary Fig. S3. At 5 K, the resistivity of $\text{Mn}_3\text{Si}_2\text{Te}_6$ drastically decreases by about

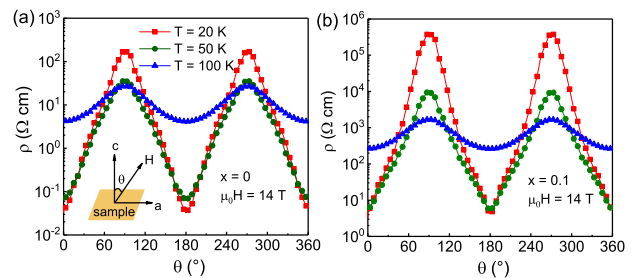


FIG. 3: (a) Angular dependence of resistivity for $\text{Mn}_3\text{Si}_2\text{Te}_6$ and (b) $(\text{Mn}_{0.9}\text{Mg}_{0.1})_3\text{Si}_2\text{Te}_6$ with $\mu_0H = 14$ T at $20, 50,$ and 100 K. The inset in (a) shows the direction of the magnetic field, where θ is the angle between H and the c axis.

8 orders of magnitude from 10^6 Ωcm at zero field to 10^{-2} Ωcm at $\mu_0H = 14$ T. The change is smaller for $(\text{Mn}_{0.9}\text{Mg}_{0.1})_3\text{Si}_2\text{Te}_6$ at 5 K. However, over a wider temperature range from 10 K to the T_C , the drop of resistivity for the doped $x = 0.1$ compound under high magnetic fields is larger. To compare the CMR as doping quantitatively, we plot $\rho(H)/\rho(0)$ as a function of the magnetic field at $10, 20,$ and 50 K below the T_C , and 100 K above the T_C in Figs. 2(c-f). Due to the limitation of the measured resistivity range, the data of the $x = 0.2$ compound at 10 and 20 K are not shown in Figs. 2(c) and 2(d). The change of the magnitude of $\rho(H)/\rho(0)$ for the doped $x = 0.1$ sample is about 2 orders larger than that of the undoped $x = 0$ sample below T_C at 14 T. The magnitudes of $\rho(H)/\rho(0)$ reverse below 6.0 T at 10 K, 2.8 T at 20 K, and 1.8 T at 50 K, respectively. The CMR effect becomes much weaker above T_C as shown in Fig. 2(f). Thermal fluctuations, SOC, and thermal activation gap are three ingredients that govern the CMR in $(\text{Mn}_{1-x}\text{Mg}_x)_3\text{Si}_2\text{Te}_6$. Increasing the temperature below T_C and strengthening the SOC will promote the conduction of electrons as expected. Our results demonstrate that substituting Mn^{2+} by nonmagnetic Mg^{2+} will enlarge the thermal activation gap, enhancing the CMR in this system.

Figure 3 shows a comparison of the colossal AMR for the undoped ($x = 0$) and doped ($x = 0.1$) compounds at 20 and 50 K below T_C , and 100 K above T_C . The AMR exhibits a two-fold rotational symmetry. The resistivity as a function of the angle of the magnetic field to the c axis evolves close to linearly, consistent with the scenario that the spins of Mn^{2+} couple with the moments of the COC along the edges of the MnTe_6 octahedra²⁵. Upon 10% Mg doping, the thermal activation gap is enlarged, and the magnitude of the AMR in $(\text{Mn}_{0.9}\text{Mg}_{0.1})_3\text{Si}_2\text{Te}_6$ is enhanced an order at the same measurement conditions. Nonetheless, it is expected that the AMR will be enhanced in a wider doping range and at lower temperatures²⁰.

Pressure can effectively tune the structure, electronic transport, and magnetism of layered structural materials^{29,31,42}. Figure 4(a) displays the high-pressure XRD patterns of $\text{Mn}_3\text{Si}_2\text{Te}_6$ up to 24.2 GPa. A clear

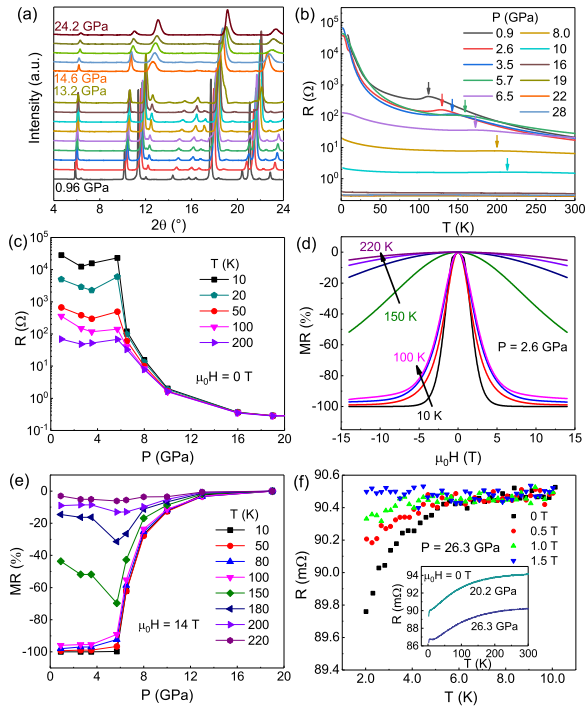


FIG. 4: (a) XRD patterns of $\text{Mn}_3\text{Si}_2\text{Te}_6$ under pressures from 0.96 to 24.2 GPa. A structural transition occurs between 13.2 and 14.6 GPa. (b) Temperature dependence of resistance of $\text{Mn}_3\text{Si}_2\text{Te}_6$ at various pressures up to 28 GPa. The Curie transition temperatures T_C s under pressure are determined from the humps on resistance marked with the arrows. (c) Pressure dependences of the resistance with $\mu_0 H = 0$ T and (e) the MR with $\mu_0 H = 14$ T at various temperatures. (d) MR defined by $(\rho_H - \rho_0)/\rho_0 \times 100\%$ at various temperatures at 2.6 GPa. (f) Resistance measurements below 10 K at 26.3 GPa and various magnetic fields. The inset shows the data from 2 to 300 K at 20.2 and 26.3 GPa with zero magnetic field. The drops of resistance at ~ 5 K and the behavior under magnetic fields indicate pressure-induced superconductivity.

structural transition is identified between 13.2 and 14.6 GPa, consistent with the reported Raman spectroscopy measurements⁴³. The XRD patterns above 14.6 GPa are consistent with the space group $C2/c$ with a monoclinic structure where the lattice constants $a = 5.682$, $b = 4.080$, $c = 11.559$ Å and $\beta = 97.88^\circ$ at 14.6 GPa. The lattice parameters as a function of pressure can be deduced from the XRD patterns (Supplementary Fig. S4). However, the accurate atomic positions cannot be determined due to the limited reflection peaks.

Under pressure, the resistance measurements reveal a semiconducting to metallic transition [Fig. 4(b)]. Below the pressure of the structural transition, the T_C can be identified as a hump in resistance, yielding a linearly increased T_C from ~ 78 K at ambient pressure to ~ 214 K at 10 GPa. The anomalous Hall effect of $\text{Mn}_3\text{Si}_2\text{Te}_6$ under pressure is intimately coupled with the magnetism (Supplementary Fig. S5). The thermal activation gap decreases with increasing pressure until closing at around 7

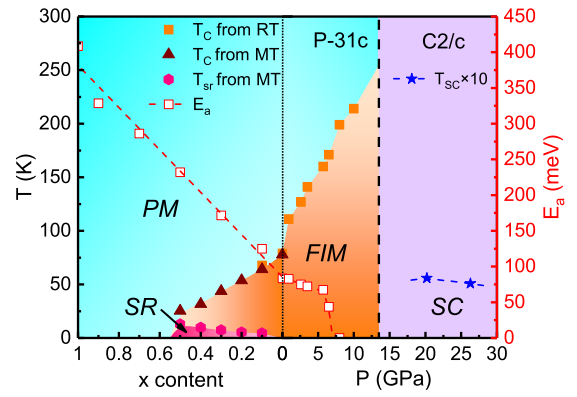


FIG. 5: A phase diagram of $(\text{Mn}_{1-x}\text{Mg}_x)_3\text{Si}_2\text{Te}_6$ against doping and pressure. The paramagnetic (PM), ferrimagnetic (FIM), spin reorientation (SR), and superconducting (SC) regions are determined by the resistance and magnetic measurements. The SC transition temperatures T_{SC} s have been magnified ten times for visualization. The thermal activation gaps, E_a s, are fitted from the resistance.

GPa. The activation gaps fitted by the polaron hopping model and the T_C s of $\text{Mn}_3\text{Si}_2\text{Te}_6$ under pressure have been presented in Fig. 5. The resistance measured at various pressures and temperatures also shows an abrupt drop at ~ 6 GPa [Fig. 4(c)]. Figure 4(d) shows typical magnetoresistance (MR defined as $(\rho_H - \rho_0)/\rho_0 \times 100\%$) measurements at 2.6 GPa and different temperatures (for more pressures, see supplementary Fig. S6). The MR shows an abrupt change across $T_C = 127$ K at 2.6 GPa [Fig. 4(d)] and a sharp drop at ~ 6 GPa [Fig. 4(e)], revealing that the SOC and thermal activation gap are the dominating ingredients that govern the MR as elevated temperature and pressure, respectively.

The resistance of $\text{Mn}_3\text{Si}_2\text{Te}_6$ at 20.2 and 26.3 GPa are shown in Fig. 4(f) to investigate the electronic property of the monoclinic structure. Clear drops can be observed below 5 K on resistance. By applying a magnetic field up to 1.5 T, the resistance at 26.3 GPa below 5 K is enhanced obviously and the drop is finally suppressed, suggesting a superconducting transition. We note that it is common for Te-contained compounds showing superconductivity under pressure, such as WTe_2 ^{44,45}, CrSiTe_3 ³², and EuTe_2 ^{30,46}, where the electrons of Te play a dominating role in superconductivity.

A comprehensive phase diagram combining the electronic, magnetic, and structural measurements as functions of doping and pressure is shown in Fig. 5. The T_C of the FIM transition decreases as doping but increases as applying pressure. The evolution of the thermal activation gap, E_a , reverses, changing from 408.6 meV in $\text{Mg}_3\text{Si}_2\text{Te}_6$ to 83.5 meV in $\text{Mn}_3\text{Si}_2\text{Te}_6$ at ambient pressure, and closing at 7 GPa. The magnetoresistance decreases dramatically as the E_a closes, revealing that the CMR of $\text{Mn}_3\text{Si}_2\text{Te}_6$ is directly coupled with E_a . The presence of magnetoresistance requires SOC that is comparable with the electronic gap. In $(\text{Mn}_{1-x}\text{Mg}_x)_3\text{Si}_2\text{Te}_6$,

the spins of Mn^{2+} possibly couple with the moments of the COC of the MnTe_6 octahedra. The superconductivity observed in the monoclinic structure under pressure may span a large pressure range.

IV. SUMMARY

In conclusion, we systematically studied the CMR, AMR, FIM, and structures of $(\text{Mn}_{1-x}\text{Mg}_x)_3\text{Si}_2\text{Te}_6$ as functions of doping and pressure. As Mn^{2+} is replaced by Mg^{2+} progressively, the FIM order is suppressed gradually until disappearing for $x > 0.5$. For the compositions with x between 0.1 and 0.5, a spin reorientation transition appears evidenced by a magnetic anomaly on magnetization at low temperatures. The thermal activation gap is enlarged linearly by the Mg doping. The CMR and AMR are both enhanced in the low-doped samples compared to the parent, which can be attributed to a doping-induced broadening of the band gap and a larger variation range of resistivity. On the contrary, T_C is enhanced with increasing pressure due to the enhanced magnetic exchange interactions until disappearing when undergoing a structural transition above 13.2 GPa. The

gap closes and a MIT occurs at ~ 7 GPa, where the CMR is abruptly reduced. A superconducting transition at 5 K in the monoclinic phase under pressure is also observed. Our finding reveals that both doping and pressure are effective methods to change the band structure and magnetism, consequently enhancing the CMR and AMR in the FIM $(\text{Mn}_{1-x}\text{Mg}_x)_3\text{Si}_2\text{Te}_6$.

V. ACKNOWLEDGMENTS

Work at Sun Yat-Sen University was supported by the National Key Research and Development Program of China (grant Nos. 2023YFA1406500, 2023YFA1406002), the National Natural Science Foundation of China (grant No. 12174454), the Guangdong Basic and Applied Basic Research Foundation (grant No. 2021B1515120015), the Guangzhou Basic and Applied Basic Research Funds (grant Nos. 2024A04J6417), and the Guangdong Provincial Key Laboratory of Magnetoelectric Physics and Devices (grant No. 2022B1212010008). We also thank the BL15U1 station in Shanghai Synchrotron Radiation Facility (SSRF) for the help in characterizations.

* Electronic address: sunhlei@mail.sysu.edu.cn

† Electronic address: wangmeng5@mail.sysu.edu.cn

- ¹ P. Grünberg, R. Schreiber, Y. Pang, M. Brodsky, and H. Sowers, *Physical Review Letters* **57**, 2442 (1986).
- ² M. N. Baibich, J. M. Broto, A. Fert, F. N. Van Dau, F. Petroff, P. Etienne, G. Creuzet, A. Friederich, and J. Chazelas, *Physical Review Letters* **61**, 2472 (1988).
- ³ J. Q. Xiao, J. S. Jiang, and C. Chien, *Physical Review Letters* **68**, 3749 (1992).
- ⁴ S. M. Thompson, *Journal of Physics D: Applied Physics* **41**, 093001 (2008).
- ⁵ I. Ennen, D. Kappe, T. Rempel, C. Glenske, and A. Hütten, *Sensors* **16**, 904 (2016).
- ⁶ B. Diény, *Journal of Magnetism and Magnetic Materials* **136**, 335 (1994).
- ⁷ R. von Helmolt, J. Wecker, B. Holzapfel, L. Schultz, and K. Samwer, *Physical Review Letters* **71**, 2331 (1993).
- ⁸ S. Jin, T. H. Tiefel, M. McCormack, R. Fastnacht, R. Ramesh, and L. Chen, *Science* **264**, 413 (1994).
- ⁹ A. Millis, B. I. Shraiman, and R. Mueller, *Physical Review Letters* **77**, 175 (1996).
- ¹⁰ Z.-C. Wang, J. D. Rogers, X. Yao, R. Nichols, K. Atay, B. Xu, J. Franklin, I. Sochnikov, P. J. Ryan, D. Haskel, et al., *Advanced Materials* **33**, 2005755 (2021).
- ¹¹ Y. Shimakawa, Y. Kubo, and T. Manako, *Nature* **379**, 53 (1996).
- ¹² P. Majumdar and P. Littlewood, *Physical Review Letters* **81**, 1314 (1998).
- ¹³ P. Rosa, Y. Xu, M. Rahn, J. Souza, S. Kushwaha, L. Veiga, A. Bombardi, S. Thomas, M. Janoschek, E. Bauer, et al., *npj Quantum Materials* **5**, 52 (2020).
- ¹⁴ J. Yin, C. Wu, L. Li, J. Yu, H. Sun, B. Shen, B. A. Frandsen, D.-X. Yao, and M. Wang, *Physical Review Materials*

- 4**, 013405 (2020).

- ¹⁵ H. Yang, Q. Liu, Z. Liao, L. Si, P. Jiang, X. Liu, Y. Guo, J. Yin, M. Wang, Z. Sheng, et al., *Physical Review B* **104**, 214419 (2021).
- ¹⁶ Z. Sun, A. Wang, H. Mu, H. Wang, Z. Wang, T. Wu, Z. Wang, X. Zhou, and X. Chen, *npj Quantum Materials* **6**, 94 (2021).
- ¹⁷ T. Ogasawara, K.-K. Huynh, T. Tahara, T. Kida, M. Hagiwara, D. Arçon, M. Kimata, S. Y. Matsushita, K. Nagata, and K. Tanigaki, *Physical Review B* **103**, 125108 (2021).
- ¹⁸ H. Vincent, D. Leroux, D. Bijaoui, R. Rimet, and C. Schlenker, *Journal of Solid State Chemistry* **63**, 349 (1986).
- ¹⁹ Y. Ni, H. Zhao, Y. Zhang, B. Hu, I. Kimchi, and G. Cao, *Physical Review B* **103**, L161105 (2021).
- ²⁰ J. Seo, C. De, H. Ha, J. E. Lee, S. Park, J. Park, Y. Skourski, E. S. Choi, B. Kim, G. Y. Cho, et al., *Nature* **599**, 576 (2021).
- ²¹ G. Sala, J. Lin, A. Samarakoon, D. Parker, A. May, and M. Stone, *Physical Review B* **105**, 214405 (2022).
- ²² C. I. Kwon, K. Kim, S. Y. Kim, R. A. Susilo, B. Kang, K. Kim, D. Y. Kim, J. Kim, B. Kim, and J. S. Kim, *Current Applied Physics* **53**, 51 (2023).
- ²³ S. D. Mijin, A. Šolajić, J. Pešić, Y. Liu, C. Petrovic, M. Bockstedte, A. Bonanni, Z. Popović, and N. Lazarević, *Physical Review B* **107**, 054309 (2023).
- ²⁴ S. W. Lovesey, *Physical Review B* **107**, 224410 (2023).
- ²⁵ Y. Zhang, Y. Ni, H. Zhao, S. Hakani, F. Ye, L. DeLong, I. Kimchi, and G. Cao, *Nature* **611**, 467 (2022).
- ²⁶ F. Ye, M. Matsuda, Z. Morgan, T. Sherline, Y. Ni, H. Zhao, and G. Cao, *Physical Review B* **106**, L180402 (2022).
- ²⁷ Q. Zhang, J. Liu, H. Cao, A. Phelan, D. Graf, J. DiTusa, D. A. Tennant, and Z. Mao, *NPG Asia Materials* **14**, 1884

- (2022).
- ²⁸ Y. Zhang, L.-F. Lin, A. Moreo, and E. Dagotto, *Physical Review B* **107**, 054430 (2023).
- ²⁹ H. Sun, L. Qiu, Y. Han, E. Yi, J. Li, M. Huo, C. Huang, H. Liu, M. Li, W. Wang, et al., *Materials Today Physics* **36**, 101188 (2023).
- ³⁰ H. Sun, L. Qiu, Y. Han, Y. Zhang, W. Wang, C. Huang, N. Liu, M. Huo, L. Li, H. Liu, et al., *Communications Physics* **6**, 40 (2023).
- ³¹ H. Sun, C. Chen, Y. Hou, W. Wang, Y. Gong, M. Huo, L. Li, J. Yu, W. Cai, N. Liu, et al., *Science China Physics, Mechanics & Astronomy* **64**, 118211 (2021).
- ³² W. Cai, H. Sun, W. Xia, C. Wu, Y. Liu, H. Liu, Y. Gong, D.-X. Yao, Y. Guo, and M. Wang, *Physical Review B* **102**, 144525 (2020).
- ³³ C. Prescher and V. B. Prakapenka, *High Pressure Research* **35**, 233 (2015).
- ³⁴ G. S. Pawley, *Journal of Applied Crystallography* **14**, 357 (1981), ISSN 0021-8898.
- ³⁵ Y. Xu, W. Li, C. Wang, Z. Chen, Y. Wu, X. Zhang, J. Li, S. Lin, Y. Chen, and Y. Pei, *Journal of Materiomics* **4**, 215 (2018).
- ³⁶ A. F. May, Y. Liu, S. Calder, D. S. Parker, T. Pandey, E. Cakmak, H. Cao, J. Yan, and M. A. McGuire, *Physical Review B* **95**, 174440 (2017).
- ³⁷ Y. Liu, C. Petrovic, et al., *Physical Review B* **98**, 064423 (2018).
- ³⁸ L. Martinez, H. Iturriaga, R. Olmos, L. Shao, Y. Liu, T. T. Mai, C. Petrovic, A. R. Hight Walker, and S. Singamaneni, *Applied Physics Letters* **116**, 172404 (2020).
- ³⁹ Y. Liu, Z. Hu, M. Abeykoon, E. Stavitski, K. Attenkofer, E. D. Bauer, C. Petrovic, et al., *Physical Review B* **103**, 245122 (2021).
- ⁴⁰ H. Liu, M. Huo, C. Huang, X. Huang, H. Sun, L. Chen, J. Xu, W. Yin, R. Li, and M. Wang, arXiv:2303.00597 (2023).
- ⁴¹ C. Huang, B. Cheng, Y. Zhang, L. Jiang, L. Li, M. Huo, H. Liu, X. Huang, F. Liang, L. Chen, et al., *Chinese Physics B* **32**, 037802 (2023).
- ⁴² R. Olmos, P.-H. Chang, P. Mishra, R. R. Zope, T. Baruah, Y. Liu, C. Petrovic, and S. R. Singamaneni, *The Journal of Physical Chemistry C* **127**, 10324 (2023).
- ⁴³ J. Wang, S. Wang, X. He, Y. Zhou, C. An, M. Zhang, Y. Zhou, Y. Han, X. Chen, J. Zhou, et al., *Physical Review B* **106**, 045106 (2022).
- ⁴⁴ X.-C. Pan, X. Chen, H. Liu, Y. Feng, Z. Wei, Y. Zhou, Z. Chi, L. Pi, F. Yen, F. Song, et al., *Nature communications* **6**, 7805 (2015).
- ⁴⁵ D. Kang, Y. Zhou, W. Yi, C. Yang, J. Guo, Y. Shi, S. Zhang, Z. Wang, C. Zhang, S. Jiang, et al., *Nature Communications* **6**, 7804 (2015).
- ⁴⁶ P. T. Yang, Z. Y. Liu, K. Y. Chen, X. L. Liu, X. Zhang, Z. H. Yu, H. Zhang, J. P. Sun, Y. Uwatoko, X. L. Dong, et al., *Nature Communications* **13**, 2975 (2022).